

Influence of pulse duration on plasma chemistry and thin film growth of plasmonic titanium nitride deposited by constant-current regulated HIPIMS

MUIR, E <<http://orcid.org/0009-0005-5513-5388>>, EHIASARIAN, Arutiun <<http://orcid.org/0000-0001-6080-3946>>, PURANDARE, Yashodhan <<http://orcid.org/0000-0002-7544-9027>>, BOWER, R <<http://orcid.org/0000-0002-3519-0532>> and PETROV, PK <<http://orcid.org/0000-0003-3643-6685>>

Available from Sheffield Hallam University Research Archive (SHURA) at:
<https://shura.shu.ac.uk/36149/>

This document is the Published Version [VoR]

Citation:






MUIR, E, EHIASARIAN, Arutiun, PURANDARE, Yashodhan, BOWER, R and PETROV, PK (2025). Influence of pulse duration on plasma chemistry and thin film growth of plasmonic titanium nitride deposited by constant-current regulated HIPIMS. *Journal of Applied Physics*, 138 (10): 105304. [Article]

Copyright and re-use policy

See <http://shura.shu.ac.uk/information.html>

RESEARCH ARTICLE | SEPTEMBER 08 2025

Influence of pulse duration on plasma chemistry and thin film growth of plasmonic titanium nitride deposited by constant-current regulated HIPIMS

E. Muir ; A. P. Ehasarian ; Y. P. Purandare ; R. Bower ; P. K. Petrov *J. Appl. Phys.* 138, 105304 (2025)<https://doi.org/10.1063/5.0273474>

Articles You May Be Interested In

High power impulse magnetron sputtering using a rotating cylindrical magnetron

J. Vac. Sci. Technol. A (December 2009)

Investigating different carbon-based target materials: Can we improve ionization in HiPIMS for the deposition of diamondlike carbon films?

J. Vac. Sci. Technol. A (May 2024)

N doped ZnO (N:ZnO) film prepared by reactive HiPIMS deposition technique

AIP Advances (March 2020)

Nanotechnology & Materials Science



Optics & Photonics



Impedance Analysis



Scanning Probe Microscopy



Sensors



Failure Analysis & Semiconductors



Unlock the Full Spectrum.

From DC to 8.5 GHz.

Your Application. Measured.

[Find out more](#)

Influence of pulse duration on plasma chemistry and thin film growth of plasmonic titanium nitride deposited by constant-current regulated HIPIMS

Cite as: J. Appl. Phys. **138**, 105304 (2025); doi: [10.1063/5.0273474](https://doi.org/10.1063/5.0273474)

Submitted: 31 March 2025 · Accepted: 12 August 2025 ·

Published Online: 8 September 2025



E. Muir,^{1,a)} A. P. Ehiasarian,¹ Y. P. Purandare,¹ R. Bower,² and P. K. Petrov²

AFFILIATIONS

¹National HIPIMS Technology Centre, School of Engineering and Built Environment, Sheffield Hallam University, United Kingdom

²Department of Materials, Imperial College London, London, United Kingdom

^{a)}Author to whom correspondence should be addressed: E.muir@shu.ac.uk

ABSTRACT

This study documents the results of an investigation into the effect of pulse duration within constant-current reactive high power impulse magnetron sputtering of titanium discharges, specifically investigating the effects on plasma chemistry and its temporal evolution and on changes to thin film texture of titanium nitride thin films produced from these discharges. Pulse durations ranging from 40 to 200 μ s were studied. The data obtained from the time-resolved optical emission spectroscopy and supported by time-resolved and time-averaged mass spectrometry show three stages that can be used to characterize the generation of the discharge: gas rarefaction, pumping, and steady state. The rise in higher excitation energy species populations when increasing pulse duration provides proof of increasing electron temperature and increasing prevalence of metal ions relative to gas ions. Increasing pulse duration is shown to strongly influence film grain sizes as determined by x-ray diffraction and increase the prominence of the (200) crystal plane. The produced films are shown to exhibit instrumental nano-hardnesses within 31–35 GPa, are optically metallic, and exhibit a high localized surface plasmon resonance quality factor of 2 as obtained from the ratio between the real and imaginary dielectric permittivity. All films were produced at room temperature making the synthesis process CMOS compatible.

© 2025 Author(s). All article content, except where otherwise noted, is licensed under a Creative Commons Attribution (CC BY) license (<https://creativecommons.org/licenses/by/4.0/>). <https://doi.org/10.1063/5.0273474>

I. INTRODUCTION

Plasmonic materials were first documented in the 1950s but have been of huge interest in the scientific community over the past decade, with substantial progress being made toward using them in a range of industrially relevant applications, including sensing,^{1–4} environmental remediation,^{5,6} photovoltaics,^{4,7} and photocatalysis.⁴ These materials have also been studied for use in photothermal therapies^{8,9} and biomedical applications.^{3,4} In the latter case, for example, nanoparticles are used to produce photocatalysing reactions which create reactive oxygen species¹⁰ as a mechanism of killing bacteria¹⁰ without eluting metal ions as is the case for traditional Ag and Cu-based materials. However, it is still poorly understood within the scientific community how to improve the environmental stability of highly plasmonic materials. For example, gold is widely used as a plasmonic material,⁴ which lacks long-term environmental stability when used in harsh and/or high

temperature environments,⁴ gold also suffers from a lack of mechanical robustness limiting its effectiveness.

Titanium nitride (TiN) is an ideal candidate for further investigation as it is a Transition-Metal Nitride (TMN) ceramic with high environmental stability, which has been shown to exhibit high metallic plasmonic activity.¹¹ In addition, it has a tunable resonance, achieved by changing the shape and size of the TiN features, capable of reacting with visible light. TiN is also ideal because of its high hardness and high wear- and corrosion resistance.^{12,13} However, high-quality plasmonically active TiN has been difficult to produce, typically requiring deposition temperatures in excess of 400 °C, because TiN is strongly influenced by the deposition conditions, being particularly sensitive to the oxygen substitution for nitrogen within its crystal lattice which can significantly alter the dielectric permittivity and plasmonic performance.¹⁴ When oxidation occurs during deposition, a TiO_x contaminant phase forms at

18 September 2025 09:20:03

grain boundaries, which limits the growth of the (111) TiN phase and fragments it into sub-columns.¹⁵ Increasing levels of oxygen within the produced film can also lead to a transition from the columnar structure to globular,¹⁶ as well as a reduction in grain size and lattice parameter,¹⁶ meaning great care must be taken to minimize oxygen contamination within the deposition chamber.

High oxygen contamination levels in TiN have been found to give rise to double Epsilon Near Zero (ENZ) points.¹⁷ Oxygen contamination can be combatted by creating TiN with a super dense microstructure, as shown by Ehasarian *et al.*,¹⁶ who used High Power Impulse Magnetron Sputtering (HIPIMS) and reported that oxygen molecules were not able to accumulate into grain boundaries and disrupt crystal growth. Instead, they were absorbed into the crystal lattice. HIPIMS grown films have been shown to have denser morphologies,^{18–23} reduced contamination,²⁴ and smoother surfaces^{19–21,25} than conventional sputtering techniques.

The majority of research conducted with HIPIMS has utilized voltage-regulated (single and multi-level) techniques,^{26–31} where the current develops and fluctuates throughout the pulse depending on the impedance of the circuit and discharge, often leading to runaway currents, particularly in reactive deposition environments. This in turn means that the plasma density will also fluctuate making it difficult to decouple plasma density and the temporal evolution of the plasma chemistry and challenging to achieve a controllable process. Since the plasma density drives the ionization processes within the discharge,³² attaining an equilibrium state within a constant voltage discharge can be very difficult. HIPIMS constant voltage plasma discharges are known to develop from gas-rich to metal-rich plasma states. While these stages are well documented and understood within non-reactive atmospheres,^{33–35} little is known about these processes within reactive depositions.

This experiment aims to create high-quality plasmonic titanium nitride by tailoring the deposition environment in order to address these issues. Achieving this goal requires a deeper understanding of how the chemistry of the plasma used during deposition influences the film growth and how the pulse duration used to generate the plasma affects the film morphology and optical properties.

The research utilizes constant-current-regulated HIPIMS to achieve exceptionally high ionization while maintaining stable operation. We show clearly the gas rarefaction phase and identify a subsequent plasma pumping stage that leads onto a steady state while the discharge current remains constant. We focus on studying plasma chemistry and electron temperature during the different stages of development of the deposition environment, and their effect on the crystallographic texture, microstructure, nanohardness, and plasmonic properties of the resulting films. To extend the applicability of the process to CMOS processing, polymers, and other heat-sensitive substrates, all depositions were conducted at room temperature.

II. EXPERIMENTAL DETAILS

A. Coater

For coating deposition, a CS400S (Von Ardenne Anlagen Technik, Germany) cluster deposition system was used. The cluster system contained a sample loading chamber, a transfer chamber, and two deposition chambers. The deposition chamber, shown

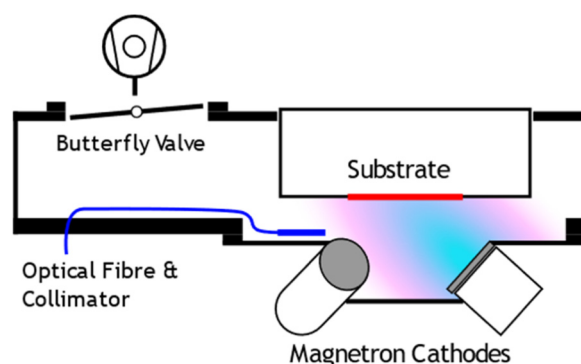


FIG. 1. Schematic cross section of the coating deposition chamber.

schematically in Fig. 1, was equipped with a magnetron furnished with a titanium target of diameter of $100 \times 10 \text{ mm}^2$ thick. The cathode was operated by a HIPIMS power supply type TruPlasma Highpulse 4002 G2 (TRUMPF Huettinger Sp. z O.O.) with a peak voltage of 2 kV and a peak current of 1 kA. The deposition chamber utilized a turbo pump with a pumping speed of $1100\text{--}1250 \text{ ls}^{-1}$ and an ultimate pressure of 1×10^{-9} mbar. The deposition process itself comprised of four stages, which were process gas flushing, pumping, target cleaning, and coating deposition.

B. Tin coating

Titanium nitride coatings were deposited onto various substrates including M2 high-speed steel (HSS) disks (30 mm diameter \times 6 mm thick), 304 stainless steel (SS) disks (30 mm diameter \times 6 mm thick), silicon wafers (10 mm \times 10 mm \times 1 mm squares), and glass plates (10 \times 10 \times 1 mm³ squares).

The glass and silicon samples were sequentially sonicated in acetone, industrial methylated spirit, and distilled water for a 3-min interval each. The high-speed steel and stainless-steel disks were metallurgically polished to a mirror finish with up to $1 \mu\text{m}$ abrasive diamond particles. HSS and SS samples were cleaned to remove oils, grease, oxidation, and contaminants. They were put through an industrial cleaning line comprising two ultrasonic tanks containing a KOH alkaline solution (3%–5%) heated to 60°C , de-ionized water, and a vacuum dryer.

A process gas flushing protocol was used prior to target cleaning, to remove gaseous contaminants from the deposition chamber, and gas pipes caused by leaks. The flushing protocol consisted of admitting argon at a flow of 90 SCCM and N_2 at 68.5 SCCM over 15 min. The flushing protocol was monitored using a differentially pumped residual gas analyzer (type MKS e-Vision 2) to ensure that O_2 , O , and CO_2 contaminations had dropped to acceptable levels of partial pressure of $<3 \times 10^{-9}$, $<3 \times 10^{-9}$, and $<2 \times 10^{-9}$ mbar, respectively.

The coatings were deposited utilizing one pure titanium target and a nitrogen and argon atmosphere. During deposition, the substrate holder was rotated at a speed of 10 rpm. All coatings were deposited at room temperature and at floating substrate bias. The

TABLE I. Conditions for target cleaning and deposition protocols.

Target cleaning	0.8 kW, 100 A, 100 μ s, 100 Hz, $t = 5-7$ min, Ar = 50 SCCM, Butterfly valve = 1.2×10^{-3} mbar				
	Deposition				
P_{average} (kW)	U (V)	I_{peak} (A)	Pulse duration (μ s)	Frequency (Hz)	Deposition time (min)
0.70	693	47.6	80	300	90
0.69	695	44.0	100	240	90
0.69	662	44.9	120	200	85.6
0.71	645	44.5	160	150	72.5
0.74	682	45.0	200	120	133

Ar and N₂ flows were kept constant at 90 and 3 SCCM, respectively. The vacuum pumping speed was varied using a throttle (butterfly) valve to maintain a pressure of 3.0×10^{-3} mbar. The peak current density was 0.57 A cm^{-2} .

Coatings were deposited using a series of five different pulse durations and frequencies (as shown in Table I). All coatings were deposited to a thickness of approximately $1 \mu\text{m}$.

To achieve a constant average power, each sample made in the series of experiments was designed to investigate the role that pulse duration and frequency had on the resulting thin film properties; therefore, in each experiment, the product of frequency and pulse duration was maintained constant at $24 \text{ kHz}\mu\text{s}$.

C. Plasma characterization

1. Time-averaged optical emission spectroscopy (OES)

Wide range emission spectra were collected using a Czerny-Turner type Horiba Jobin Yvon FHR1000 optical emission spectrometer, which was connected to the deposition chamber using a quartz fiber optic cable and utilized a Sincerity CCD detector. Species and transitions used for analyses are summarized in Table II.

The data shown in Table II for the wavelength, transition levels, terms, and energy levels of Ar⁰, Ar¹⁺, Ti⁰, and Ti¹⁺ were found on the National Institute of Standards and Technology's Atomic

Spectral Database.³⁶ The data for N₂ (e.g., the transition levels, terms, and energy levels) were found in two publications.^{37,38}

2. Time-resolved OES

Time-resolved OES measurements were taken of the previously specified species (Table II) using a Horiba PMT R955 photomultiplier detector whose output was shunted to ground through a $10 \text{ k}\Omega$ resistor and recorded using a digital oscilloscope type MSO54 (Tektronix). Time-resolved OES was conducted for each pulse duration investigated. Discharge parameters were measured using a Tektronix P5100A voltage probe ($100\times$ attenuation) and a Pearson 110 current monitor ($10\times$ attenuation).

3. Mass spectrometry

A PSM003 plasma-sampling energy-resolved mass spectrometer (Hidden Analytical Ltd.) was used to record time-averaged and time-resolved measurements of the ion flux arriving at the substrate. Time-resolved measurements were synchronized with the voltage on-time. A Multi-Channel Scaler (MCS) facility of the spectrometer was used to allow high-speed time-resolved analysis of the monitored ions by counting the number of ions arriving at the detector during the channel time. Mass spectroscopy was conducted by replacing the substrate holder and substrate with a flange-mounted mass spectrometer. The plasma-sampling orifice of the instrument was positioned at the center of the substrate position and at the same height. A temporal resolution of $5 \mu\text{s}$ was used.

It is known that for mass spectrometers the transmission and detection of the ions reduces with mass-to-charge ratio. This means that the absolute ion concentrations underestimate the heavier species detected, however, when comparing species with similar mass such as Ti¹⁺ (47.9) and Ar¹⁺ (40) or Ti²⁺ (24), N₂ (28) and Ar²⁺ (20) are close enough.

D. Coating characterization

1. XRD

X-ray Diffraction (XRD) data were collected using an X'PERT-PRO system (Panalytical), which was equipped with a copper source operated at a voltage of 40 kV and current of 40 mA as well as a nickel β filter and a collimator placed before the

TABLE II. Summary of species investigated.

Species ion/spectrum	Wavelength λ (nm)	Transition levels	Terms	Energy levels (eV)
Ar ⁰ /Ar I	811.531 1	$3s^2 3p^5(^2P^{\circ}_{3/2})4s-3s^2 3p^5(^2P^{\circ}_{3/2})4p$	$^2[3/2]^{\circ}-^2[5/2]$	11.6–13.1
Ar ¹⁺ /Ar II	440.098 6	$3s^2 3p^4(^3P)3d-3s^2 3p^4(^3P)4p$	$^4D-^4P^{\circ}$	16.4–19.2
N ₂	390.295 6	$v'' = 0-v' = 0$	$N_2^+(X^2\Sigma_u^+)-N_2^+(B^2\Sigma_u^+)$	0.0–3.16
Ti ⁰ /Ti I	365.349 49	$3d^2 4s^2-3d^2(^3F)4s4p(^1P^{\circ})$	$a^3F-y^3G^{\circ}$	0.048–3.44
Ti ⁰ /Ti I	499.106 70	$3d^3(^4F)4s-3d^3(^4F)4p$	$a^5F-y^5G^{\circ}$	0.836–3.32
Ti ⁰ /Ti I	521.038 40	$3d^2 4s^2-3d^2(^3F)4s4p(^3P^{\circ})$	$a^3F-z^3F^{\circ}$	0.048–2.43
Ti ¹⁺ /Ti II	334.883 95	$3d^3-3d^2(^3F)4p$	$b^4F-z^4F^{\circ}$	0.122–3.82
Ti ¹⁺ /Ti II	375.929 15	$3d^2(^3F)4s-3d^2(^3F)4p$	$a^2F-z^2F^{\circ}$	0.607–3.90
Ti ¹⁺ /Ti II	327.891 86	$3d^2(^1D)4s-3d^2(^1D)4p$	$a^2D-z^2P^{\circ}$	1.08–4.87

18 September 2025 09:20:03

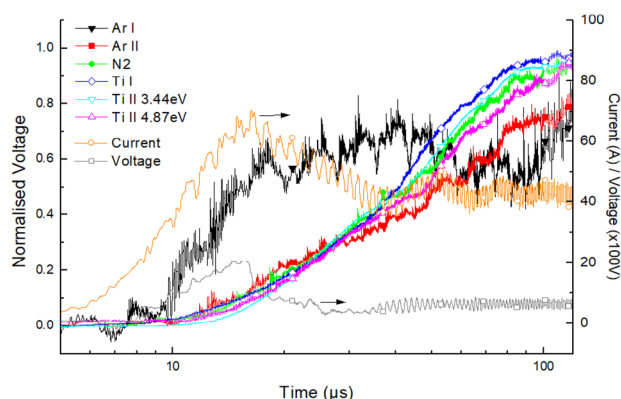


FIG. 2. Overlaid time-resolved OES log plot readings for the generation of species, discharge voltage, and discharge current within the initial stages of a pulse with duration of 200 μ s.

detector. XRD scans were conducted using a multi-purpose sample stage (MPSS) plate holder over the range 20°–120° with a step size of 0.013 13°. The background was removed from each XRD scan using Highscore Plus software.

2. XRD texture

The pole figures were collected using a Malvern Panalytical Empyrean system, which was equipped with a cobalt source operated at a voltage of 40 kV and current of 40 mA as well as an iron β filter. The incident and diffracted angles (Ω and 2θ) were kept at 21° and 42°, respectively, while the tilt (ψ) and azimuth (φ) were varied in the range 0°–85° and 0°–360°, respectively.

3. Ball cratering

Ball cratering was conducted to measure the film thickness, using a CSEM Calowear microabrasion tester with a ball diameter of 30 mm and 1 μ m diamond paste.

4. Ellipsometry

Optical properties and dielectric function of the films were collected using a JA Woollam V-VASE spectroscopic ellipsometer. Ellipsometric parameters ψ and δ were collected with incident angles of 65°, 70°, and 75°, and the dielectric permittivity of the TiN thin films were extracted by fitting to a Drude–Lorentz model consisting of one Drude oscillator and two Lorentz oscillators (see the Appendix). It is worth noting that as these TiN films are approximately 1 μ m thick, metallic, and, therefore, absorbing, measurements do not probe the full depth of the films. The steel substrate has, therefore, not been included in the model as due to the film thickness, the contribution from this layer is negligible. The TiN film has been treated as a semi-infinite layer. To account for surface roughness of the film, an additional layer was added to the ellipsometry fitting model, consisting of an effective medium composed of equal parts TiN and air.

III. RESULTS

A. Plasma generation (TR OES)

The time-resolved OES data shown in Figs. 2 and 3 illustrate how the plasma discharge develops over the duration of the pulse. Figure 2 focuses on the initial stages of the pulse and shows clearly that the first species to develop is Ar neutral (marked by black inverted triangle) which develop quickly but then saturate at around 20 μ s. At 50 μ s, the Ar neutral species intensity drops and a rapid increase in Ar II emission (line marked by red squares) is

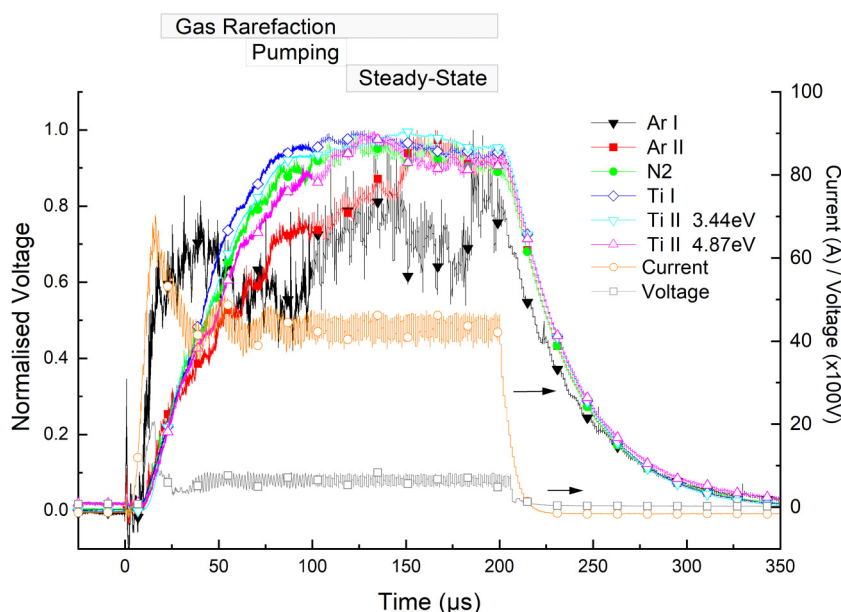


FIG. 3. Overlaid time-resolved OES readings for the generation of species, discharge voltage, and discharge current within a 200 μ s pulse.

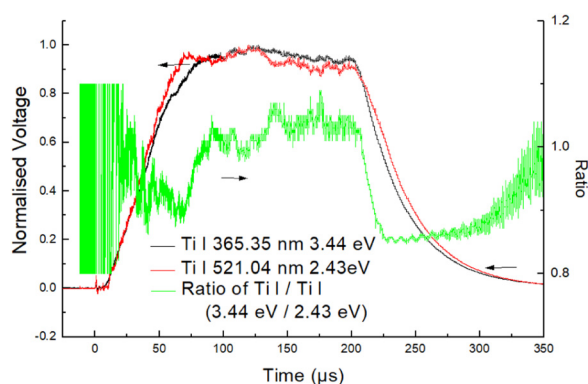


FIG. 4. A graph used to analyze electron temperature of the plasma by comparing two Ti I excitation levels.

observed, both of which could be attributed to the combined effect of gas rarefaction and the ionization of Ar neutrals. Figure 2 shows the successive appearance of Ti I and Ti II emissions as ions are created from neutrals. The ion emission increases faster and catches up with the neutral at $\sim 25 \mu\text{s}$, after which they both develop together. At around $50 \mu\text{s}$, Ti neutrals (as shown by the dark blue hollow diamond line) rise rapidly and are followed by a stable and continuous emission of Ti II ions (see light blue hollow diamond line for lower excitation Ti II and magenta hollow triangle line for higher excitation energy Ti II), which increase in population while the discharge current remains constant between ~ 60 and $200 \mu\text{s}$ (for current waveform see hollow orange circle line in Fig. 3); this indicates a lack of equilibrium within the system. The voltage (see hollow gray square line in Fig. 3) has an initial spike reaching peak voltage at approximately $20 \mu\text{s}$ and then settles into a near-constant voltage at approximately $40 \mu\text{s}$ lasting to the end of the pulse.

Figure 4 shows the temporal evolution of two Ti I levels with different excitation energies throughout the pulse. The two levels investigated are Ti I found at 365.37 nm (black square line) and Ti I found at 521.06 nm (red circle line) which have excitation energies of 3.44 and 2.43 eV , respectively. The ratio of the higher energy level against the lower energy level was calculated (green triangle line) as a means of direct analysis of electron temperature as demonstrated by Ricard *et al.*³⁹ and Zhu *et al.*⁴⁰ As shown in Fig. 4 by the green line, after $\sim 60 \mu\text{s}$, the electron temperature increases and reaches a steady state at $\sim 120 \mu\text{s}$.

B. Plasma chemistry (TA OES)

As seen in Fig. 5, important changes in the emissions of Ti I and Ti II lines are recorded when pulse duration is changed. A Ti I line (2.43 eV) found at 521.03 nm is shown to decrease with increasing pulse duration, whereas a higher excitation energy Ti I line (3.32 eV) found at 499.09 nm is shown to increase with increasing pulse duration, which qualitatively shows that the electron temperature of the system is increasing with increasing pulse

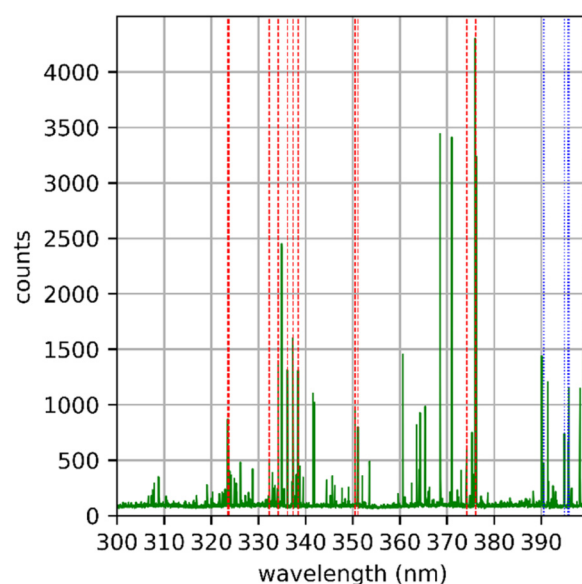


FIG. 5. OES scan taken for a pulse duration of $80 \mu\text{s}$ identifying Ti neutrals and Ti single ions. Neutral emission lines are marked by the red dashed lines which inhabit the range of $320\text{--}380 \text{ nm}$. Single ion emission lines are marked with blue dotted lines inhabiting the range of $390\text{--}400 \text{ nm}$.

duration. Ar I lines are shown to have a near-constant intensity regardless of the duration of the pulse.

Figure 6 shows that the populations of species of Ti with the lower excitation energy are decreasing while the higher energy species are increasing when pulse duration is increased. Since all

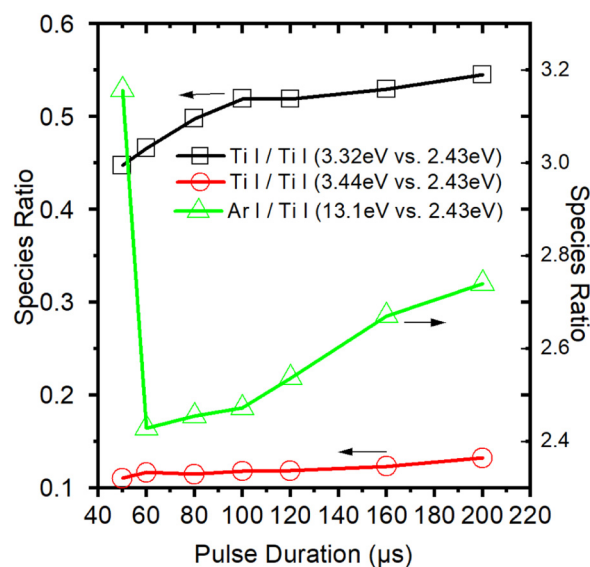


FIG. 6. Species ratios for different pulse durations.

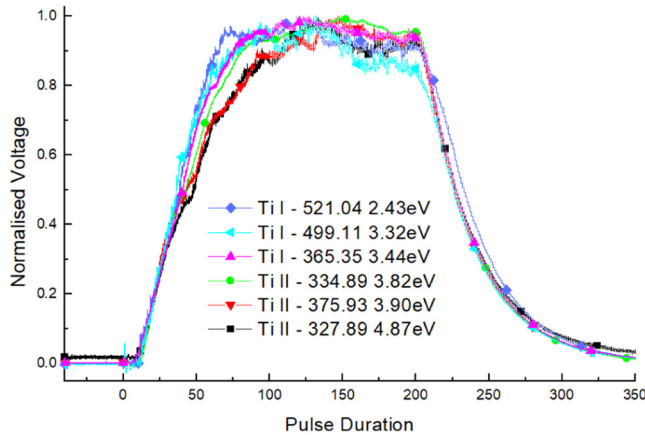


FIG. 7. Plot comparing the generation of multiple titanium species with different upper excitation level energies as indicated.

pulse durations have similar peak power and average power, the relative increase in higher energy populations could be attributed to an increase in electron temperature throughout the pulse duration interval: faster up to $100\mu\text{s}$ and slower beyond that. The Ar I/Ti I ratio is also shown to rise as pulse duration surpasses $60\mu\text{s}$ due to higher energy excitation levels of Ar I species becoming more populated as pulse duration increases caused by a rising electron temperature. Since the excitation energy of Ar I is a factor of 2 greater than Ti I (see Table II), the increase in line ratio indicates that with higher pulse duration, the electron temperature increases, assuming the same density ratios. This assumption is reasonable as density fluctuations are relatively small in the body of the pulse beyond the

ignition and pumping phase. The Ar I/Ti I ratio also depends on the temperature of the species. For the density of Ti, the time-resolved data (Figs. 3, 4 and 7) suggest that the intensity of Ti emissions is either increasing or at a steady state, and there is no evidence of reduction due to excessive ionization. At the same time, the Ar density is likely to reduce with increasing pulse duration as the sputtered metal continues to maintain and enhance gas rarefaction. The increase in Ti and the reduction of Ar densities would drive a reduction in the Ar I/Ti I ratio, which is contrary to the data observed.

During the initial phase of gas rarefaction, the density of Ar collapses quickly. The first point of the Ar I/Ti I plot in Fig. 6 at $50\mu\text{s}$ has a value of above 3 and does not fit the rest of the trend but can be explained by a change in the density ratio of the species caused by the gas rarefaction following the initial production of gas plasma (see Fig. 3 to compare Ar I to all other species).

Despite mass spectroscopy measurements (see Fig. 9) and literature indicating that HIPIMS can produce doubly ionized metal species, including Ti^{2+} , no emission from such species was detected using OES during this study.⁴¹ The lack of doubly ionized species is due to either or both the low oscillator strength and/or the overlap these species have with other titanium species, making them difficult to identify.

From Fig. 7, the emission from the lowest energy neutral species of titanium (2.43 eV) identified develops first within the plasma as expected, which is subsequently shortly followed by the generation of two titanium neutral species with higher excitation energies (3.32 and 3.44 eV, respectively). Ti^{1+} are created from Ti neutrals, then the first ionic species (3.82 eV) develop quickly after the neutrals; however, after a delay of a few microseconds, two higher energy ionic species (3.90 and 4.87 eV) begin to develop. Due to the fast current rise of the HIPIMS pulse, there is little delay to the generation of ions; however, there is a delay between ions and

18 September 2025 09:20:03

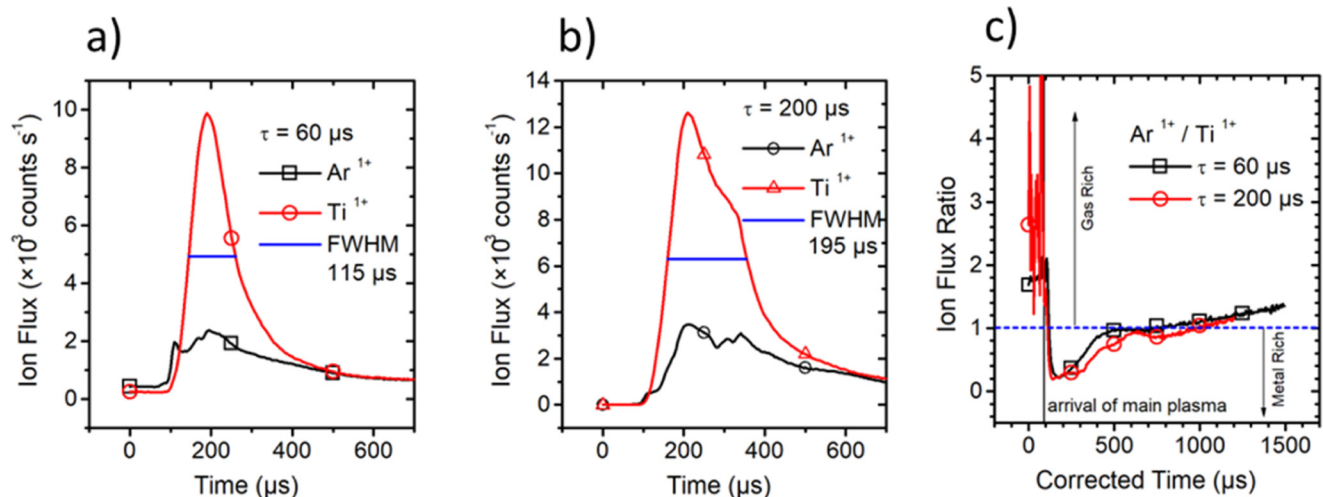


FIG. 8. Shows ion flux measurements taken from time-resolved mass spectrometry measurements. (a) Shows Ar^{1+} and Ti^{1+} during a $60\mu\text{s}$ pulse. (b) Shows Ar^{1+} and Ti^{1+} during a $200\mu\text{s}$ pulse. (c) Shows the ratio $\text{Ar}^{1+}/\text{Ti}^{1+}$ for both the 60 and $200\mu\text{s}$ pulse durations.

neutrals that was indicated in the discussion of Fig. 2. Ti^{1+} and Ti^{2+} ions are created through successive ionization from neutrals, having ionization potentials of 6.82 and 13.58 eV, respectively, both lower than that of Ar, thereby making them very likely to occur.

The lowest energy titanium neutral signal saturates at roughly 70 μs , followed by the two higher energy neutral species which saturate at 90 μs . The three singly ionized titanium species saturate at almost the same time at roughly 145 μs and do so in order of lowest to highest excitation energy.

C. Mass spectrometry

Figure 8(a) shows the ion flux measured at the substrate position, for Ar^{1+} and Ti^{1+} during a 60 μs pulse. Ar^{1+} rises quickly and has an initial peak before the arrival of Ti^{1+} shortly after. The Ar^{1+} level then drops and then slowly rises again to peak at 200 μs . The ion fluxes of both species peak at the same time. The decay of Ar^{1+} is significantly slower than the rapid decay of Ti^{1+} . Figure 8(b)

shows the same fluxes for a 200 μs pulse, where a similar temporal evolution can be seen again, but with Ti^{1+} arriving with no measurable delay to Ar^{1+} . Ar^{1+} fluxes increase by 50% and Ti^{1+} by roughly 20%, giving evidence for higher electron temperatures. For the 200 μs pulse, there is a definitive change in the shape of the decay of Ti^{1+} and Ar^{1+} with a shoulder appearing at roughly 300 μs for both ionic species at the same point in time, which results in a slower decay than that of the 60 μs pulse, measured from the peak ion flux. Overall, the metal flux pulse extended by a factor of approximately 70% from 60 to 200 μs . Figure 8(a) shows that Ti^{1+} in the 60 μs pulse has a narrower Full Width Half Maximum (FWHM) of 115 μs and an ion flux of 4.94×10^4 , whereas Fig. 8(b) shows Ti^{1+} within the 200 μs pulse to have a wider FWHM of 195 μs and a higher ion flux of 6.3×10^4 .

For both Figs. 8(a) and 8(b), the flux reaches a maximum after the duration of the pulse, which is caused in part by the flight time taken for the ions to reach the mass spectrometer and due to the remaining high energy ions being able to escape the target

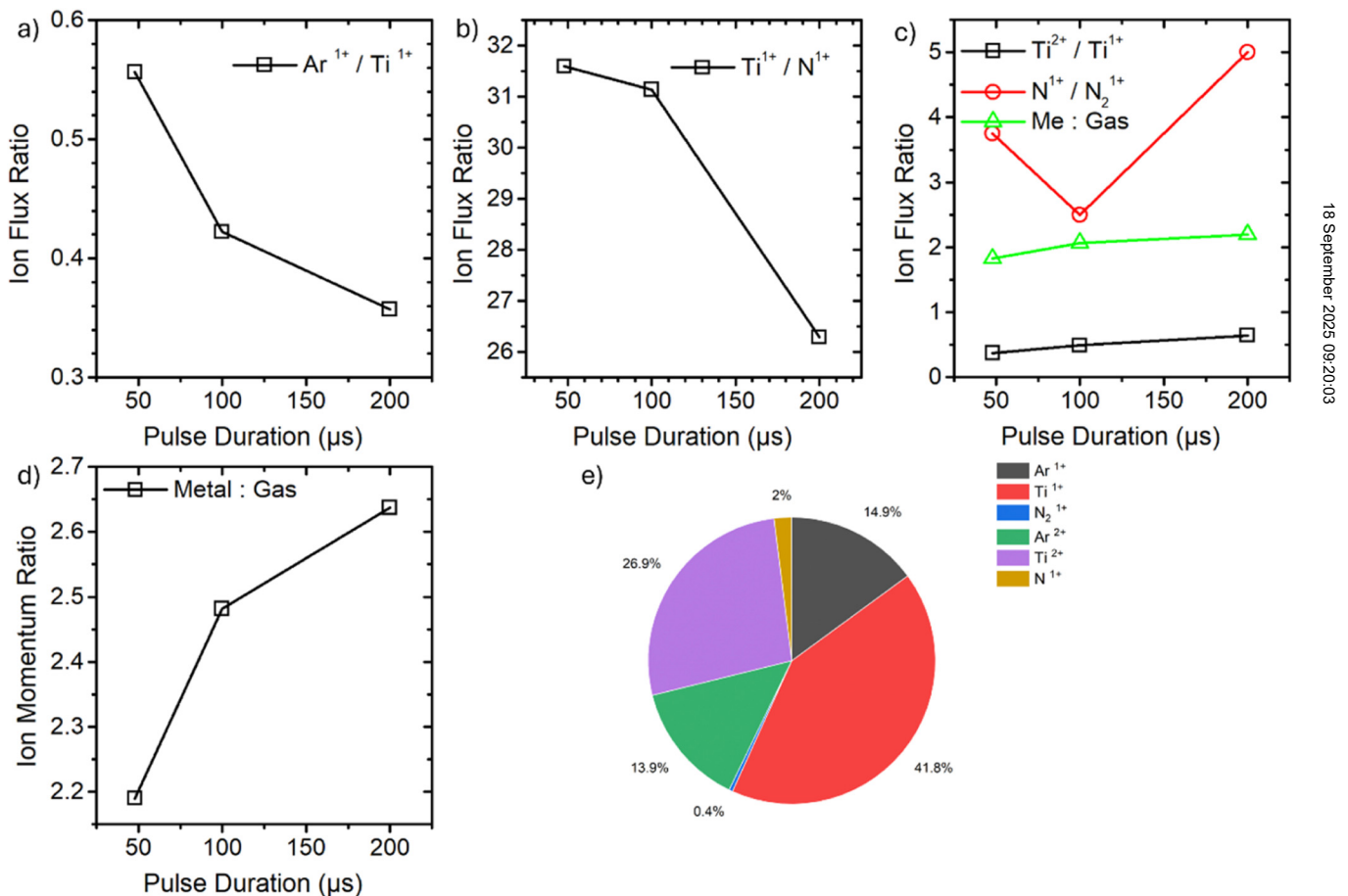


FIG. 9. Shows data measured at three different pulse durations from time-averaged mass spectrometry. (a) Shows the ion flux ratio of $\text{Ar}^{1+}/\text{Ti}^{1+}$. (b) Shows the ion flux ratio of $\text{Ti}^{1+}/\text{N}^{1+}$. (c) Displays ion flux ratios for $\text{Ti}^{2+}/\text{Ti}^{1+}$, $\text{N}^{1+}/\text{N}_2^{1+}$, and metal/gas. (d) Shows the ion momentum ratio for metal/gas. (e) Displays the percentage ion flux signal for all species within the 200 μs discharge.

when the discharge ends.⁴² The Ar^{1+} flux has also been shown in previous studies of HIPIMS discharges to have a pronounced peak following the termination of the pulse.⁴³

Figure 8(c) shows the comparison between the $\text{Ar}^{1+}/\text{Ti}^{1+}$ ratios during the 60 and 200 μs pulses. Both pulses follow the same pattern of an initial immediate rise, resulting in a gas phase, and the subsequent drop in the ratio, indicating the beginning of a metal-rich phase happens at the same point in time for both. By estimating the difference in flight delay for Ar^{1+} and Ti^{1+} within the spectrometer, as approximately 5 μs , adjusting the ion flux ratios for each pulse duration shows that these ratios reach 1.00 (± 0.05) at 480 and 950 μs for the 60 and 200 μs pulse, respectively. The difference in flight delay was approximated based on previous calculations for the same mass spectrometer in a previous study.⁴⁴ Figure 8(c), therefore, shows that the longer duration pulse results in a substantially longer metal-rich phase, lasting approximately 840 μs , compared to the shorter duration pulse which lasts approximately 360 μs .

The long decay time of the order of ms of Ar^{1+} following a HIPIMS pulse observed here agrees with previous studies.^{43,44}

Comparison of mass spectroscopy results with the published literature and this study is rather complex as previous studies focus on voltage-regulated discharges with slow ramping currents,^{42,43,45} which results in very different developments of ion flux which experiences phases of peaks and valleys throughout the discharge which is not the case in these results as the current remains constant for a large proportion of the discharge.

Figure 9(a) shows that at lower pulse durations, there is a higher level of Ar^{1+} compared to Ti^{1+} , then as the pulse duration is increased to its maximum duration, the ratio drops by 36%. Figure 9(b) shows that the ratio of $\text{Ti}^{1+}/\text{N}^{1+}$ is at a maximum at lower pulse durations and decreases as the pulse duration is increased, from the maximum value to the lowest value the ratio is reduced by 17%. Although the absolute ratio is underestimated due to the large difference in mass-to-charge ratio of the two species, the change in the ratio is correct. Figure 9(c) shows how the ion flux ratio for $\text{Ti}^{2+}/\text{Ti}^{1+}$ slowly rises continuously with increasing pulse duration and the same is seen with the metal/gas ion flux ratio. Interestingly, the atomic to molecular nitrogen ion flux ratio does not follow this same behavior, when increasing from 50 to 100 μs , there is a 33% reduction in the amount of N^{1+} ; however, when increasing the pulse duration from 100 to 200 μs , there is a 100% increase in N^{1+} . Figure 9(d) shows the ion momentum ratio for metal against gas within the discharge, the ratio rises continuously as the length of the pulse is increased, with a total increase of 23% from lowest to highest pulse duration. Figure 9(e) shows the percentage ion flux signals for all species within the 200 μs discharge, where the most populous species is Ti^{1+} with 42%, followed by Ti^{2+} which represents 27%. Ar^{1+} and Ar^{2+} represent 15% and 14%, respectively. Ionized dissociated nitrogen has a content of 2% and finally, the smallest population is the ionized molecular nitrogen with 0.4%.

D. Film texture

XRD analysis was conducted to evaluate the effect of increasing pulse duration on the crystallographic texture of the films and

determine if the film growth was in a preferred direction. XRD was conducted on the thin films produced in the pulse duration series; therefore, there were five sets of XRD scans and pole figures for crystal planes identified from the XRD analysis. The crystallographic planes identified on the samples from XRD, as shown in Fig. 10, were (111), (200), (220), and (311). (111) and (200) were identified in all samples with the former being the most prominent followed by the latter. All peaks present in the figure which are not labeled belong to the substrate, 304 stainless steel.

From analyzing the XRD data (see Fig. 10) from the produced samples, the patterns indicate that a single-phase TiN was grown under all pulse duration conditions. A texture coefficient derived from the ratio of diffraction peak area divided by relative intensity against the sum of all diffraction peak areas divided by relative intensities allows the identification of the most prominent crystal plane-parallel to the surface [see Fig. 11(a)]. The XRD traces reveal a trend that by increasing the pulse duration of the deposition, there is an increase in area for the (200) diffraction peaks. Figure 10 shows that samples produced at lower pulse durations have more mixed crystallographic texture, whereas the high pulse duration samples have reduced or no (220) and (311) planes orientated along the surface normal, only (111) and (200) planes. For the (111) and (200) peaks, as pulse duration is increased, the peaks decrease in intensity; however, there is also evidence of broadening. Broadening of peaks is caused by microstrain within the film,⁴⁶ which could be a result of lattice defects and reduction in grain size. As seen in Fig. 10, there is also a noticeable shift in some of the peaks when comparing samples from different pulse durations, for example, when comparing the

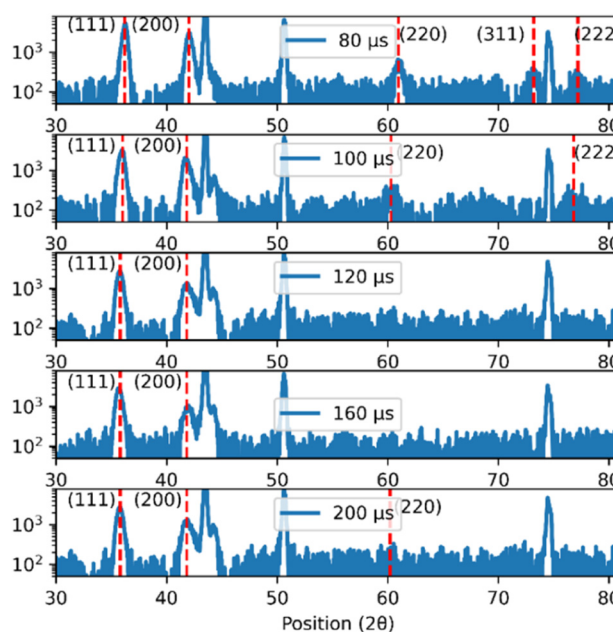


FIG. 10. XRD plots for samples created at different pulse durations, crystal planes for TiN have been identified with a dashed line and labeled with the corresponding plane.

18 September 2025 09:20:03

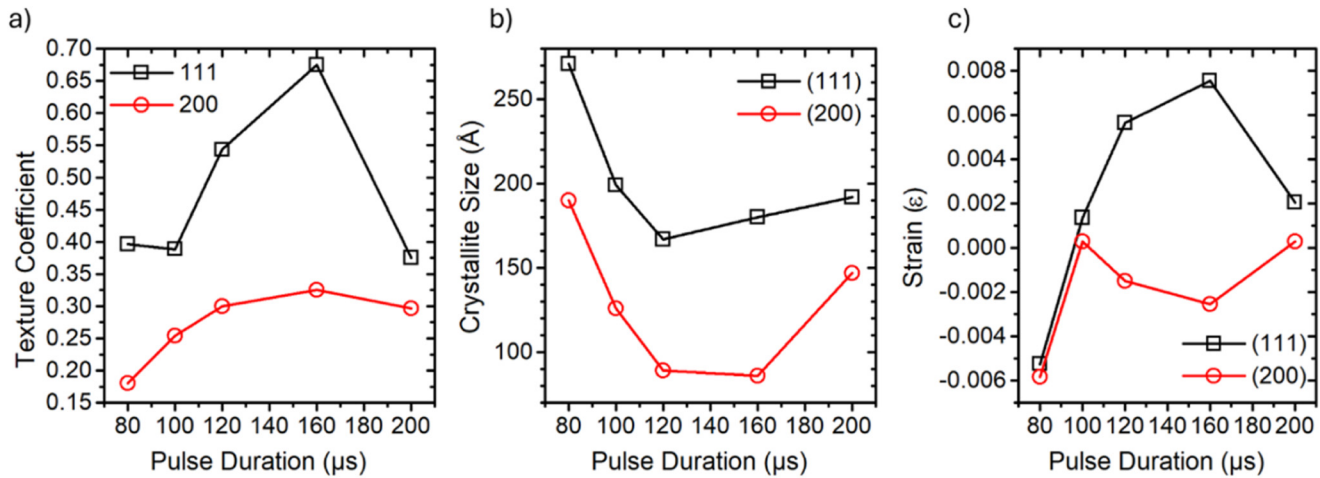


FIG. 11. (a) Texture coefficients of (111) and (200) for a range of pulse durations. (b) (111) and (200) crystallite sizes for each pulse duration. (c) (111) and (200) strain values for each pulse duration.

(111) peak from the 50 μs sample to the samples produced at pulse durations of 120, 160, and 200 μs, this shift in peak position is caused by uniform stress which extends over the bulk of the film.⁴⁶ From Fig. 10, there is a visible peak at 44° 2θ for all samples, which in the first plot is low intensity, this peak is identified as iron ferrite within the stainless-steel substrate.

Figure 11(b) and Table III show the crystallite sizes for (111) and (200) for each pulse duration, and crystallite sizes for both (111) and (200) are the largest at the lowest pulse duration. For (111), crystallite sizes decreased with increasing pulse duration from 80 until 120 μs; however, from 120 to 200 μs, there is a gradual increase. For (200), crystallite sizes decreased with increasing pulse duration from 80 to 160 μs but increased significantly in size at 200 μs. Figure 11(c) shows the strain in (111) and (200) orientated crystallites obtained by comparing measured crystallite peak positions to recorded standard measurements as per Eq. (1),

$$\varepsilon = \frac{d_f^{(hkl)} - d_{\text{standard}}^{(hkl)}}{d_{\text{standard}}^{(hkl)}}. \quad (1)$$

Both crystallites have negative strains at 80 μs. The (111) crystallite increases continuously from 80 to 160 μs where it then drops

sharply at 200 μs. For (200), the samples produced at 80, 120, and 160 μs are nearly unstrained or slightly negative, with only the 100 and 200 μs samples exhibiting positive strains.

Comparing the pole figures for the shortest and longest pulse in Fig. 12, the shorter pulse can be seen to have a weaker texture in both the (111) and (200) planes, which is consistent with low energy ion bombardment.⁴⁷ The short duration pulses created samples with a more mixed and random crystallographic texture. In contrast, the longer duration pulses created samples with a less random texture, with more prominent central intensities for the (111) and (200) planes. The narrowing of central intensities indicates larger grain sizes.

E. Hardness and toughness

Figure 13(a) shows that the TiN samples produced on stainless steel have nano-hardnesses within the range of 31.5–34.9 GPa. Figure 13(b) shows that the toughness determined from the H^3/E^2 ratio of these samples ranges from 0.207 to 0.301 GPa. From Figs. 13(a) and 13(b), both the lowest sample hardness and toughness are produced at the lowest pulse duration, and both values then continue to increase until they reach a maximum at 160 μs.

TABLE III. Peak position and crystallite sizes for (111) and (200) grains of samples made under different pulse durations determined from XRD and average roughness (R_a) from profilometry.

Pulse duration (μs)	Peak position (111)	Crystallite size (Å)	Peak position (200)	Crystallite size (Å)	Average R_a (nm)
80	36.199	271	42.009	190	29.3 ± 3.5
100	35.920	199	41.772	126	20.9 ± 9.6
120	35.745	167	41.864	89	18.5 ± 4.8
160	35.670	189	41.920	86	24.0 ± 3.1
200	35.898	192	41.778	147	50.5 ± 8.9

18 September 2025 09:20:03

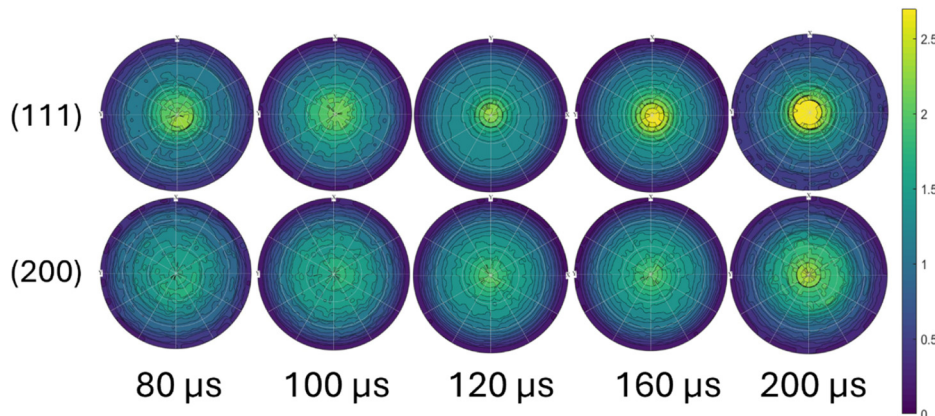


FIG. 12. Pole figures of the (111) and (200) planes from all samples.

From 160 to 200 μs , however, there is a decrease in both hardness and toughness.

F. Ellipsometry

As indicated in Fig. 14, all titanium nitride thin films are optically metallic, with a negative real permittivity across much of the visible and IR, spectral range, consistent with the literature.^{11,48–50} See Fig. 15 for ellipsometry parameters Ψ and Δ . There is little variation in the crossover wavelength (475 ± 2 nm) indicating consistent stoichiometry, further supported by the golden color observed in the films.⁵¹ Some variations in the real and imaginary dielectric permittivity are observed at longer wavelengths, however. At these wavelengths, the optical properties of TiN arise due to intraband absorption, the interaction of light with the conduction electrons. The intraband transitions are dependent upon the electron mean free path and, therefore, grain size of TiN. Slight variations in grain size and morphology may account for the differences in the optical properties at red and infrared wavelengths.

In addition to the real and imaginary permittivity, one can assess the suitability of transition-metal nitride thin films for plasmonic applications using the localized surface plasmon resonance

quality factor (Q_{LSPR}). This can be obtained by comparing the ratio between the real and imaginary dielectric permittivity $[-\text{Re}(\epsilon)/\text{Im}(\epsilon)]$ and can be used as a first approximation to assess the suitability of these films for plasmonic applications.⁵² It should be noted that this figure-of-merit does not consider particle geometry or its interaction with the environment and more robust assessments are possible, as outlined by Doiron *et al.*¹⁷ There is slight variation in Q_{LSPR} between films deposited with different pulse durations, with 80 and 200 μs outperforming films deposited with other pulse durations.

IV. DISCUSSION

A. Plasma generation

Figure 3 shows a clear progression from gas dominated to metal-dominated plasma. Three distinct stages can be identified to characterize the generation of the plasma: gas rarefaction, pumping, and steady state. The gas rarefaction and steady state stages of HIPIMS discharges have been well documented in the published literature;^{34,53–55} however, the presence of the pumping stage may not have been apparent until constant-current discharges could be analyzed.

At 20 μs , the discharge current drops, indicating a reduction in plasma density. This coincides with a drop in voltage as well as the generation of metal emission lines which both result in reduction of electron temperature due to lower electric field strength and absorption of high energy electrons, respectively. Both the reduction in density and electron temperature limits the rise of Ar neutral emissions. Gas rarefaction can be seen in Fig. 3 up until around 60 μs , at roughly 40 μs , there is a continuous drop in the Ar neutral signal, pointing to a reduction in the density of Ar neutrals, while there is simultaneously a continued increase in the signal intensity for the sputter material neutrals and ions. This shows that while the Ar neutrals are being pushed away from the target, more sputtered material is being released. Gas rarefaction can be identified from the reduction in density of neutrals in front of the target, which is caused by the sputtered metal ions pushing the neutrals away.^{34,56} Gas rarefaction continually occurs throughout the duration of the pulse.

18 September 2025 09:20:03

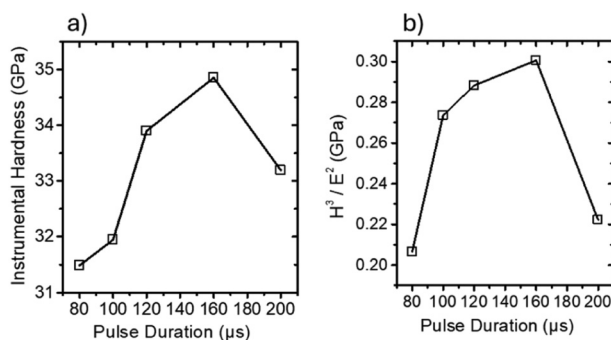


FIG. 13. Influence of HIPIMS pulse duration on (a) nano hardness and (b) toughness (H^3/E^2) of TiN.

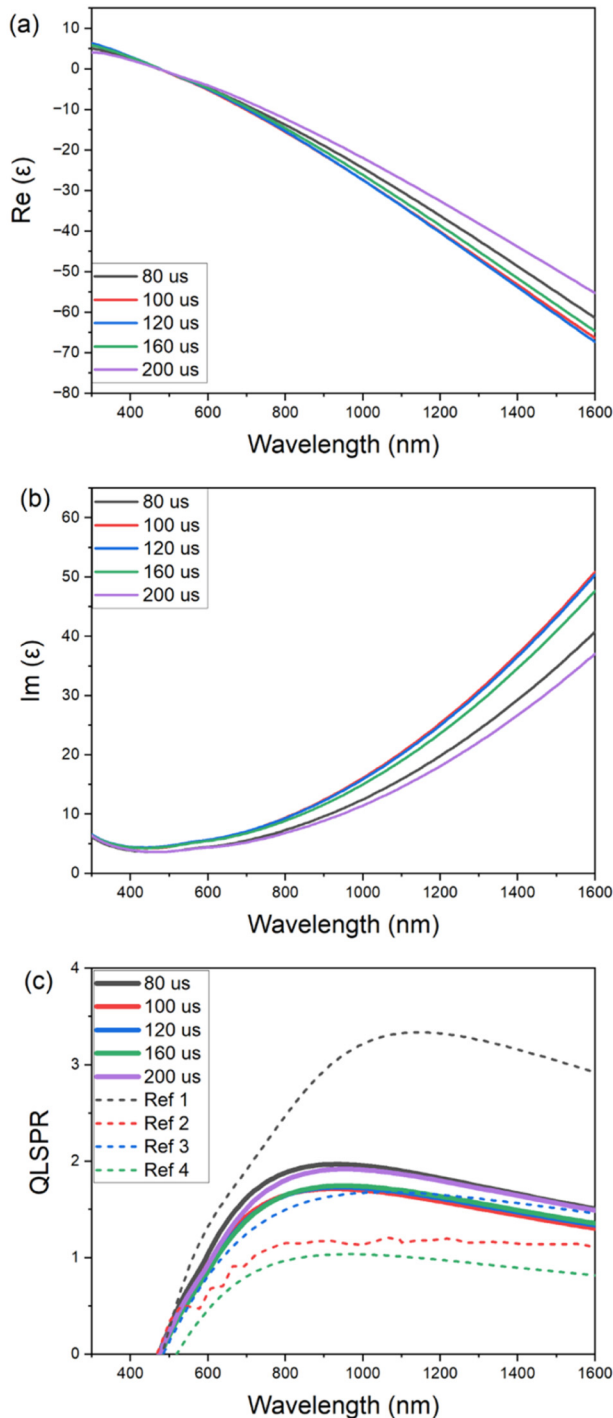


FIG. 14. Real (a) and imaginary (b) permittivity of TiN films deposited with different HIPIMS pulse durations, extracted from spectroscopic ellipsometry data. (c) Localized surface plasmon resonance quality factor (QLSPR), a typical figure-of-merit for plasmonic materials, for TiN thin films deposited with different pulse durations.

Figure 3 shows that during the pumping stage, initially, the current fluctuates down at $\sim 50 \mu\text{s}$, while the voltage remains constant, implying an expansion of the cathode sheath due to lower plasma density and reduction of the electric field within the sheath. In the same timeframe, optical emission signals (Fig. 3) indicate that the electron temperature increases. This increase could be associated with electrons being accelerated by the expanding cathode sheath and in the pre-sheath. Pumping proceeds as sufficient ionization occurs; the high density of free electrons leads to an increased rate of collisions and subsequently results in an increase in the probability of ionization. This leads to the formation of larger ion populations and an increase in electron temperature.

Around $50 \mu\text{s}$, there is a steady increase in the Ar II signal (Fig. 3), showing that Ar neutrals are being ionized at a faster rate, which is evidence of an increased probability of ionization and indicative of the pumping stage. After $60 \mu\text{s}$, the rate of rise of Ti neutral and ion emissions slows down. By roughly $90 \mu\text{s}$, Ti neutral emissions reach a steady level but despite this, the emissions for both Ti II lines continue to increase until roughly $120 \mu\text{s}$. This effect on the sputtered material is indicative of the pumping stage as higher energy states such as Ti II are increasingly populated because of a higher probability of ionization given by an increase in the rate of collisions and electron temperature. Steady state occurs after $\sim 120 \mu\text{s}$ where the metal populations dominate and the electron energy cools, reducing the gas neutral population.

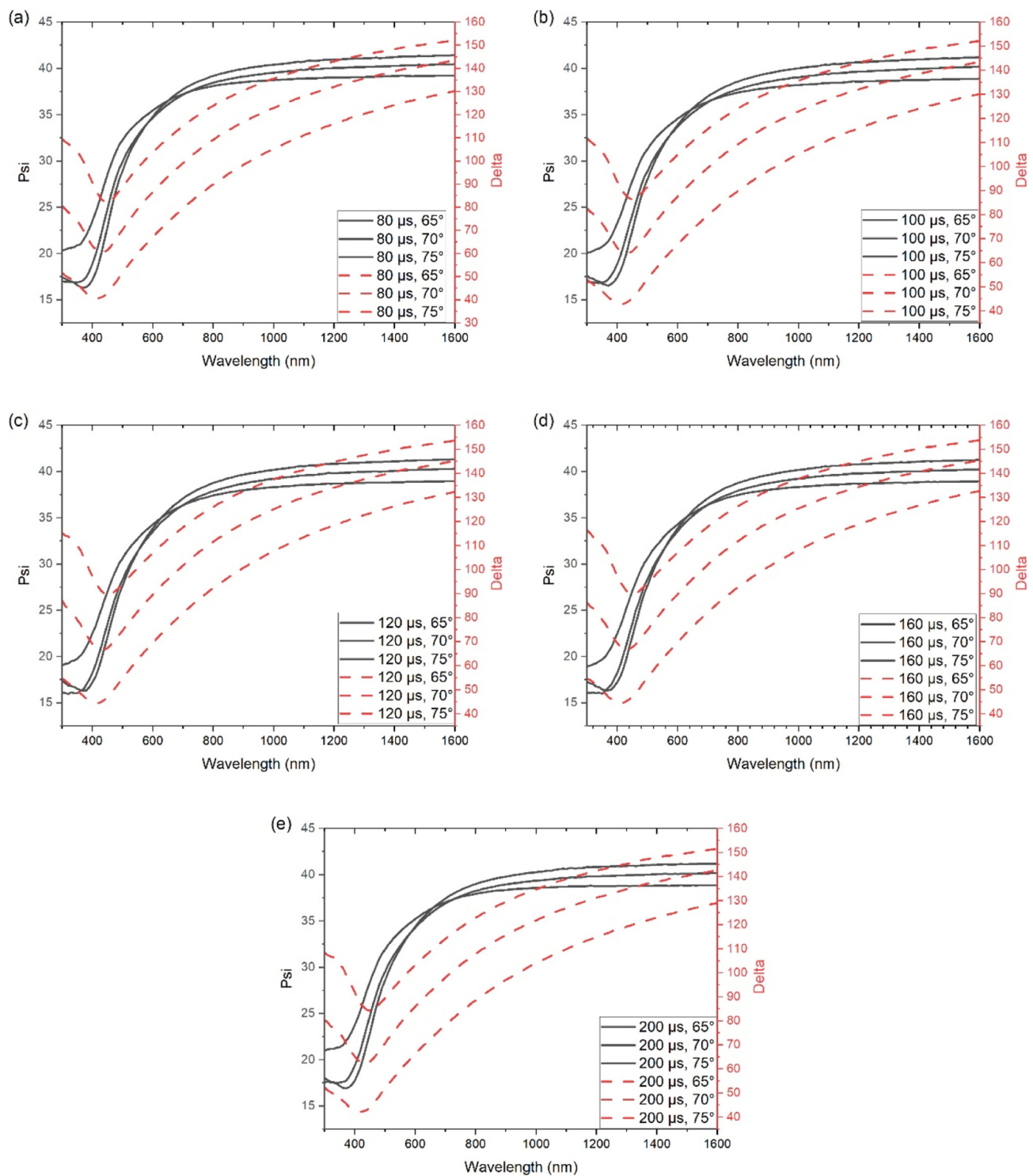
B. Plasma chemistry

The gas-to-metal ion flux ratios to the substrates shown in Fig. 8(c) develop from a short gas-rich phase, which is rapidly replaced with a metal-rich phase. The plasma chemistry development at the substrate appears to originate at the target as supported by the data conveyed on Fig. 6, where the neutral emission ratios for Ar I/Ti I appear to follow the same trend of a high value, that then drops significantly followed by a slow subsequent rise. Overall, it is remarkable that the constant-current HIPIMS appears to maximize the metal ion bombardment by almost eliminating the time differential between metal and gas ion species for their initial arrival and their peak value. Gas is associated with higher stress; the new approach eliminates it.

C. The interplay between deposition conditions and coating microstructure, and mechanical and optical properties

The grain size of the films was strongly influenced by the pulse duration. Up to $160 \mu\text{s}$, the longer pulse duration created samples with broader diffraction peaks and smaller grain size. This correlates well with the plasma conditions outlined in Secs. III A–III C, which show that as the pulse develops, the electron temperature increases, thereby enhancing the ionization rate and the ion-to-neutral ratio. Ions accelerate while traversing toward the substrate pre-sheath and experience further acceleration inside the sheath itself, thereby arriving at the substrate with intrinsically higher energy than neutrals. The higher energetic bombardment appears to have contributed to reducing the grain size and increasing the strain in the lattice as shown in Figs. 11(b) and 11(c). Both effects are known to enhance the hardness of materials and support our observation of an

18 September 2025 09:20:03



18 September 2025 09:20:03

FIG. 15. Ellipsometry parameters Ψ and Δ collected using spectroscopic ellipsometry with an angle of incidence of 65°, 70°, and 75° for TiN samples with pulse lengths of (a) 80, (b) 100, (c) 120, (d) 160, and (e) 200 μs .

increased instrumental hardness and toughness of the films [Figs. 13(a) and 13(b)]. Throughout this range of pulse durations, the texture remains a preferred (111), thereby inducing changes in grain size and strain within the same crystal orientation.

Throughout the pulse duration series, there is a continuous substantial reduction in Ar^{1+} relative to metal ion bombardment [Fig. 9(a)], an increase in the presence of activated (atomic) nitrogen relative to metal ions [Fig. 9(b)], and an increase in the momentum contributed by the metal ions compared to gas ions [Fig. 9(d)]. Overall, constant-current HIPIMS discharges are reported to produce metal ion species that on average have higher energies than the inert gas ions produced by conventional discharges.⁴¹

The XRD peak analysis in Fig. 11(a) and pole figure results in Fig. 12 show a trend that as pulse duration is increased, the (200) grains increase in prominence by nearly double from 80 to 200 μs so that the overall texture approaches a randomly orientated distribution of grains. Longer pulse durations lead to greater populations of metallic species as well as greater populations of high energy excitation states. This is further supported by the fact that the films produced in this study have larger grain sizes and a higher prevalence of the (200) crystallographic planes, which are indicative of higher energy adatoms.⁴⁷

Contributing to this switch could be the increase in atomic nitrogen flux relative to titanium, which could trap metal onto (200) surfaces.⁵⁷ The prevalence of (200) surfaces is known to reduce contaminant buildup at grain boundaries in favor of absorption in the lattice in the bulk of the grains.⁵⁸ This unblocks the diffusion of coating adatoms into grain boundaries and supplies the required flux to densify them. Overall, this could explain the larger grain size for the films deposited at $t = 200 \mu\text{s}$ observed by XRD [Fig. 11(b)]. The replacement of Ar ion with metal ion bombardment [Fig. 9(d)] could reduce the generation of lattice defects, as seen by the lower strain of films deposited at $t = 200 \mu\text{s}$ [Fig. 11(c)]. It is also an important contributor to increasing the grain size of the films. On the other hand, the reduced strain also lowers the hardness and toughness of the films [Figs. 13(a) and 13(b)].

The optical properties correlate well with the grain size in the films. The Q_{LSPR} of films deposited with pulse durations of 80 and 200 μs outperform films deposited with other pulse durations. The same two films also exhibit the largest grains in the series. It could be argued that grain boundaries act as scattering centers which hinder the propagation of plasmonic waves by introducing discontinuity in the free electron cloud.

TiN thin films deposited via HIPIMS with different pulse duration display Q_{LSPR} comparable to some of the best TiN reported in the literature, as demonstrated in Fig. 14(c). Chang *et al.*⁵⁹ achieved high Q_{LSPR} using RF sputtering technique, in which the RF field is responsible for increasing the temperature of electrons in the plasma and formation of a high ion density and a high ion-to-neutral flux to the substrates, which ensures high adatom mobility during deposition and a dense microstructure. A disadvantage of the method is the difficulty in upscaling while retaining uniformity due to the tendency for RF plasma to form localized regions of ionization and locally enhanced target erosion and heat dissipation on large area targets. Similar quality of films has been reported under temperatures of 750 °C in epitaxially

grown films on MgO single-crystal substrates⁶⁰ and TiN films deposited epitaxially on sapphire substrates display significantly improved Q_{LSPR} . Here, the high temperature of deposition ensures high adatom mobility and dense, high-purity films. However, a disadvantage of this approach is the incompatibility with microelectronic fabrication environments and with heat-sensitive substrates such as polymers.^{59,60} The films reported in this work are comparable with TiN films deposited using HIPIMS at CMOS compatible temperatures (300 °C) by Bower *et al.*,⁶¹ irrespective of pulse duration. Mascaretti *et al.*⁶² were able to produce TiN films with Q_{LSPR} between 0.9 and 1.3 by varying substrate bias [the unbiased results are shown in Fig. 14(c)]. Nieborek *et al.*⁶³ produced TiN films using pulsed DC discharges, while varying Ar and N_2 flow rate and pressure, where they were able to produce 1 μm thick films that achieved maximum Q_{LSPR} values ranging from 1.2 to 2.5, which also compare favorably with the films produced in this investigation.

V. CONCLUSIONS

This work demonstrates the production of high-quality, plasmonically active binary transition-metal nitride thin films at room temperature using high power impulse magnetron sputtering. The optical film performance achieved with the technology compares favorably with the best examples in the literature,^{11,50,59,61–64} while permitting production onto temperature sensitive substrates such as polymer web.

Extensive plasma diagnostics reveal high fluxes of atomic nitrogen ions and a metal-rich deposition flux, containing highly energetic doubly charged metal ions. Time-resolved measurements reveal that the discharge undergoes gas rarefaction followed by a plasma pumping stage where enhanced electron temperature drives increases in excitation and ionization in the pre-sheath while the total plasma density is maintained constant until finally a metal-rich steady state is reached. The substrate ion flux chemistry gradually shifts toward more metal ion bombardment and elevated atomic nitrogen ratios as the pulse duration is increased. Initially, this leads to increased strain and hardness of the films. At the highest pulse durations, it results in texture shifts toward (200) which promote strain relaxation, increase in grain size, and reduction in hardness. The plasmonic performance was dependent on grain size, with the largest grains providing the best conditions for plasmon generation. The optimal combination of robustness and optical performance was achieved under high atomic nitrogen and metal-dominated environment created by the longest pulses.

The scalable technology will allow large-scale deployment of robust plasmonic materials which could potentially be used as photocatalysts for antimicrobial materials, photothermal therapies, photovoltaic energy production, or environmental remediation.

ACKNOWLEDGMENTS

The authors gratefully acknowledge financial support from Engineering and Physical Sciences Research Council (EPSRC) (Grant No. EP/W009501/1). We also gratefully acknowledge support from EPSRC through the EPSRC grant (No. EP/W012197/1) and the Nanoscale Advanced Materials Engineering (NAME) Program Grant (No. EP/V001914/1). We are grateful for support from the

TABLE IV. Drude–Lorentz fitting parameters for TiN films deposited with varied pulse durations.

Pulse duration (μs)	Mean squared error	ε_∞	E_{pu} (eV)	Γ_D	E_1 (eV)	f_1	γ_1 (eV)	E_2 (eV)	f_2	γ_2 (eV)	ENZ (nm)	ε_2 @ENZ	Surface roughness (nm)
80	7.3	1	7.45	0.45	5.95	6.15	3.52	2.20	0.04	0.31	473	3.7	4.9
100	5.0	1	8.08	0.52	6.33	7.53	3.65	2.25	0.06	0.41	476	4.4	7.8
120	3.2	1	8.09	0.51	6.43	7.75	3.88	2.25	0.11	0.59	478	4.3	5.7
160	3.1	1	7.89	0.50	6.37	7.39	4.03	2.23	0.12	0.61	478	4.4	4.5
200	5.3	1	7.09	0.46	5.64	5.57	3.53	2.18	0.07	0.47	474	3.6	3.8

Henry Royce Institute made through EPSRC grant (No. EP/R00661X/1). For the purpose of open access, the author has applied a Creative Commons Attribution (CC BY) license to any Author Accepted Manuscript version arising from this submission.

AUTHOR DECLARATIONS

Conflict of Interest

The authors have no conflicts to disclose.

Author Contributions

E. Muir: Conceptualization (equal); Data curation (equal); Formal analysis (lead); Investigation (equal); Methodology (equal); Validation (equal); Visualization (lead); Writing – original draft (lead); Writing – review & editing (equal). **A. P. Ehasarian:** Conceptualization (equal); Data curation (supporting); Formal analysis (supporting); Funding acquisition (lead); Investigation (equal); Methodology (equal); Project administration (lead); Validation (equal); Visualization (supporting); Writing – original draft (supporting); Writing – review & editing (equal). **Y. P. Purandare:** Investigation (supporting). **R. Bower:** Formal analysis (supporting); Investigation (supporting); Methodology (supporting); Validation (equal); Visualization (supporting); Writing – original draft (supporting); Writing – review & editing (supporting). **P. K. Petrov:** Funding acquisition (supporting); Project administration (supporting); Writing – review & editing (supporting).

DATA AVAILABILITY

The data that support the findings of this study are available from the corresponding author upon reasonable request.

APPENDIX: SPECTROSCOPIC ELLIPSOMETRY MODELING

Ellipsometry data were fit using a Drude–Lorentz model of the form,

$$\varepsilon'(\omega) + i\varepsilon''(\omega) = \varepsilon_\infty - \frac{\omega_{pu}^2}{\omega^2 - i\Gamma_D} + \sum_{j=1}^n \frac{f_j \omega_{0j}^2}{\omega_{0j}^2 - \omega^2 + i\gamma_j \omega}, \quad (\text{A1})$$

where ε_∞ relates to background absorption and ω_{pu} and Γ_D are the unscreened plasma frequency and Drude broadening. The Lorentz oscillators are defined by the oscillator energy, strength, and

damping; ω_j , f_j , and γ_j , respectively. A single Drude oscillator and a total of two Lorentz oscillators were used as fitting parameters. An additional effective medium layer consisting of equal parts TiN and air was included in the fitting model to account for surface roughness (Table IV).

REFERENCES

- S. Khani and P. Rezaei, “Optical sensors based on plasmonic nano-structures: A review,” *Heliyon* **10**(24), e40923 (2024).
- W. Peng, B. Huang, X. Huang, H. Song, and Q. Liao, “A flexible and stretchable photonic crystal sensor for biosensing and tactile sensing,” *Heliyon* **8**(11), e11697 (2022).
- J. Cai, Y. Liu, and X. Shu, “Long-period fiber grating sensors for chemical and biomedical applications,” *Sensors* **23**(1), 542 (2023).
- B. N. Günaydin, A. O. Çetinkaya, M. Torabfam, A. Tütüncüoğlu, C. I. Kyalan, M. K. Bayazit *et al.*, “Plasmonic group IVB transition metal nitrides: Fabrication methods and applications in biosensing, photovoltaics and photocatalysis,” *Adv. Colloid Interface Sci.* **333**, 103298 (2024).
- M. E. King, C. Wang, M. V. Fonseca Guzman, and M. B. Ross, “Plasmonics for environmental remediation and pollutant degradation,” *Chem. Catal.* **2**(8), 1880–1892 (2022).
- D. Wang, S. C. Pillai, S. H. Ho, J. Zeng, Y. Li, and D. D. Dionysiou, “Plasmonic-based nanomaterials for environmental remediation,” *Appl. Catal. B* **237**, 721–741 (2018).
- H. Xie, Q. Hu, J. Huang, M. Liu, P. Wei, Y. Xie *et al.*, “Enhancing photovoltaic performance of carbon-based perovskite solar cells by introducing plasmonic Au NPs,” *Opt. Mater.* **146**, 114509 (2023).
- P. Singh, A. Sarkar, N. Mukherjee, and A. Jaiswal, “Herceptin-conjugated plasmonic gold nanocapsules for targeted NIR-II photothermal therapy,” *RSC Pharm.* **2**(1), 124–134 (2025).
- Q. Xie, T. Sun, L. Zhang, M. Gong, W. Zhang, X. Liu *et al.*, “Responsive plasmonic hybrid nanorods enables metabolism reprogramming via cuproptosis-photothermal combined cancer therapy,” *Biomaterials* **315**, 122971 (2025).
- Y. Tang, H. Sun, Z. Qin, S. Yin, L. Tian, and Z. Liu, “Bioinspired photocatalytic ZnO/Au nanopillar-modified surface for enhanced antibacterial and antiadhesive property,” *Chem. Eng. J.* **398**, 125575 (2020).
- R. Bower, D. A. L. Loch, A. Berenov, B. Zou, P. Hovsepian, A. P. Ehasarian *et al.*, “Transition metal nitride thin films deposited at CMOS compatible temperatures for tunable optoelectronic and plasmonic devices,” *arXiv:2005.05185* (2020).
- H. Gao, B. Zhang, P. Yang, Z. Wang, N. Zhou, and D. Wei, “Mechanical and tribological properties related on the texture of TiN films regulated via HiPIMS,” *Chem. Phys. Lett.* **829**, 140738 (2023).
- P. E. Hovsepian, A. A. Sugumaran, Y. Purandare, D. A. L. Loch, and A. P. Ehasarian, “Effect of the degree of high power impulse magnetron sputtering utilisation on the structure and properties of TiN films,” *Thin Solid Films* **562**, 132–139 (2014).

18 September 2025 09:20:03

- ¹⁴B. Doiron, Y. Li, R. Bower, A. Mihai, S. Dal Forno, S. Fearn *et al.*, “Optimizing hot electron harvesting at planar metal–semiconductor interfaces with titanium oxynitride thin films,” *ACS Appl. Mater. Interfaces* **15**(25), 30417–30426 (2023).
- ¹⁵D. Biro, M. F. Hasaneen, L. Székely, M. Menyhárd, S. Gurbán, P. Pekker *et al.*, “Texture change of TiN films due to anisotropic incorporation of oxygen,” *Vacuum* **103**, 78–86 (2014).
- ¹⁶A. P. Ehasarian, A. Vetushka, Y. A. Gonzalvo, G. Sáfrán, L. Székely, and P. B. Barna, “Influence of high power impulse magnetron sputtering plasma ionization on the microstructure of TiN thin films,” *J. Appl. Phys.* **109**(10), 104314 (2011).
- ¹⁷B. Doiron, M. Mota, M. P. Wells, R. Bower, A. Mihai, Y. Li *et al.*, “Quantifying figures of merit for localized surface plasmon resonance applications: A materials survey,” *ACS Photonics* **6**(2), 240–259 (2019).
- ¹⁸M. P. Ferreira, D. Martínez-Martínez, J. B. Chemin, and P. Choquet, “Tuning the characteristics of Al₂O₃ thin films using different pulse configurations: Mid-frequency, high-power impulse magnetron sputtering, and their combination,” *Surf. Coat. Technol.* **466**, 129648 (2023).
- ¹⁹F. Magnus, A. S. Ingason, O. B. Sveinsson, S. Olafsson, and J. T. Gudmundsson, “Morphology of TiN thin films grown on SiO₂ by reactive high power impulse magnetron sputtering,” *Thin Solid Films* **520**(5), 1621–1624 (2011).
- ²⁰A. Ferrec, J. Keraudy, S. Jacq, F. Schuster, P. Y. Jouan, and M. A. Djouadi, “Correlation between mass-spectrometer measurements and thin film characteristics using dcMS and HiPIMS discharges,” *Surf. Coat. Technol.* **250**, 52–56 (2014).
- ²¹H. Elmkhah, F. Attarzadeh, A. Fattah-alhosseini, and K. H. Kim, “Microstructural and electrochemical comparison between TiN coatings deposited through HiPIMS and DCMS techniques,” *J. Alloys Compd.* **735**, 422–429 (2018).
- ²²A. P. Ehasarian, P. E. Hovsepian, L. Hultman, and U. Helmersson, “Comparison of microstructure and mechanical properties of chromium nitride-based coatings deposited by high power impulse magnetron sputtering and by the combined steered cathodic arc/unbalanced magnetron technique,” *Thin Solid Films* **457**(2), 270–277 (2004).
- ²³A. Ghailane, M. Makha, H. Larhlimi, and J. Alami, “Design of hard coatings deposited by HiPIMS and dcMS,” *Mater. Lett.* **280**, 128540 (2020).
- ²⁴A. Anders, “A review comparing cathodic arcs and high power impulse magnetron sputtering (HiPIMS),” *Surf. Coat. Technol.* **257**, 308–325 (2014).
- ²⁵C. L. Chang, S. G. Shih, P. H. Chen, W. C. Chen, C. T. Ho, and W. Y. Wu, “Effect of duty cycles on the deposition and characteristics of high power impulse magnetron sputtering deposited TiN thin films,” *Surf. Coat. Technol.* **259**, 232–237 (2014).
- ²⁶V. O. Oskirko, M. V. Shandrikov, A. P. Pavlov, A. N. Zakharov, M. I. Azhgikhin, and A. A. Solov'yev, “The dynamics of the electron temperature and density in short-pulse HiPIMS discharge,” *Vacuum* **230**, 113672 (2024).
- ²⁷X. Ding, M. Cui, Y. Lian, J. Jiao, J. Yang, J. Zhang *et al.*, “Control of the preferential orientation and properties of HiPIMS and DCMS deposited chromium coating based on bias voltage,” *Vacuum* **227**, 113386 (2024).
- ²⁸J. Hnilica, P. Souček, M. Ondryáš, P. Klein, M. Fekete, and P. Vašina, “Exploring different approaches of multipulse HiPIMS,” *Surf. Coat. Technol.* **496**, 131670 (2025).
- ²⁹A. R. Shugurov, A. Y. Derbin, and E. D. Kuzminov, “Effect of the pulse frequency on the structure, mechanical and tribological properties of Ti–Al–Ta–N coatings deposited by HiPIMS,” *Vacuum* **230**, 113636 (2024).
- ³⁰Š. Batková, J. Čapek, J. Rezek, R. Čerstvý, and P. Zeman, “Effect of positive pulse voltage in bipolar reactive HiPIMS on crystal structure, microstructure and mechanical properties of CrN films,” *Surf. Coat. Technol.* **393**, 125773 (2020).
- ³¹J. Zgheib, L. Berthelot, J. Tranchant, N. Ginot, M. P. Besland, A. Caillard *et al.*, “Electron-enhanced high power impulse magnetron sputtering with a multilevel high power supply: Application to Ar/Cr plasma discharge,” *J. Vac. Sci. Technol. A* **41**(6), 063003 (2023).
- ³²A. P. Ehasarian, A. Vetushka, A. Hecimovic, and S. Konstantinidis, “Ion composition produced by high power impulse magnetron sputtering discharges near the substrate,” *J. Appl. Phys.* **104**(8), 083305 (2008).
- ³³K. Macák, V. Kouznetsov, J. Schneider, U. Helmersson, and I. Petrov, “Ionized sputter deposition using an extremely high plasma density pulsed magnetron discharge,” *J. Vac. Sci. Technol. A* **18**(4), 1533–1537 (2000).
- ³⁴A. P. Ehasarian, R. New, W. D. Münz, L. Hultman, U. Helmersson, and V. Kouznetsov, “Influence of high power densities on the composition of pulsed magnetron plasmas,” *Vacuum* **65**(2), 147–154 (2002).
- ³⁵N. Britun, S. Konstantinidis, and R. Snyders, “An overview on time-resolved optical analysis of HiPIMS discharge,” *Plasma Processes Polym.* **12**(9), 1010–1027 (2015).
- ³⁶A. Kramida, Y. Ralchenko, J. Reader and NIST ASD Team, “NIST Atomic Spectra Database (version 5.12),” available at <https://www.nist.gov/pml/atomic-spectra-database> (2024).
- ³⁷W. H. J. Childs, “Perturbations and rotation constants of some first negative nitrogen bands,” *Proc. R. Soc. London Ser. A* **137**(833), 641–661 (1932).
- ³⁸V. Linss, H. Kupfer, S. Peter, and F. Richter, “Determination of the neutral gas temperature of nitrogen-containing low-pressure plasmas using a two-temperature model,” *Surf. Coat. Technol.* **200**(5–6), 1696–1701 (2005).
- ³⁹A. Ricard, S. Oh, J. Jang, and Y. K. Kim, “Quantitative evaluation of the densities of active species of N₂ in the afterglow of Ar-embedded N₂ RF plasma,” *Curr. Appl. Phys.* **15**(11), 1453–1462 (2015).
- ⁴⁰X. M. Zhu and Y. K. Pu, “Optical emission spectroscopy in low-temperature plasmas containing argon and nitrogen: Determination of the electron temperature and density by the line-ratio method,” *J. Phys. D: Appl. Phys.* **43**(40), 403001 (2010).
- ⁴¹A. Hecimovic and A. P. Ehasarian, “Temporal evolution of the ion fluxes for various elements in HiPIMS plasma discharge,” *IEEE Trans. Plasma Sci.* **39**(4), 1154–1164 (2011).
- ⁴²W. Breilmann, C. Maszl, A. Hecimovic, and A. von Keudell, “Influence of nitrogen admixture to argon on the ion energy distribution in reactive high power pulsed magnetron sputtering of chromium,” *J. Phys. D: Appl. Phys.* **50**(13), 135203 (2017).
- ⁴³C. Maszl, W. Breilmann, J. Benedikt, and A. von Keudell, “Origin of the energetic ions at the substrate generated during high power pulsed magnetron sputtering of titanium,” *J. Phys. D: Appl. Phys.* **47**(22), 224002 (2014).
- ⁴⁴A. Hecimovic and A. P. Ehasarian, “Time evolution of ion energies in HiPIMS of chromium plasma discharge,” *J. Phys. D: Appl. Phys.* **42**(13), 135209 (2009).
- ⁴⁵P. Y. Jouan, L. Brizoual, L. Ganciu, M. Cardinaud, C. Tricot, S. Djouadi, and M. A., “HiPIMS ion energy distribution measurements in reactive mode,” *IEEE Trans. Plasma Sci.* **38**(11), 3089–3094 (2010).
- ⁴⁶S. Dolabella, A. Borzi, A. Dommann, and A. Neels, “Lattice strain and defects analysis in nanostructured semiconductor materials and devices by high-resolution x-ray diffraction: Theoretical and practical aspects,” *Small Methods* **6**(2), 2100932 (2022).
- ⁴⁷I. Petrov, P. B. Barna, L. Hultman, and J. E. Greene, “Microstructural evolution during film growth,” *J. Vac. Sci. Technol. A* **21**(5), S117–28 (2003).
- ⁴⁸P. Patsalas, N. Kalfagiannis, and S. Kassavetis, “Optical properties and plasmonic performance of titanium nitride,” *Materials* **8**(6), 3128–3154 (2015).
- ⁴⁹G. V. Naik, J. L. Schroeder, X. Ni, A. V. Kildishev, T. D. Sands, and A. Boltasseva, “Titanium nitride as a plasmonic material for visible and near-infrared wavelengths,” *Opt. Mater. Express* **2**(4), 478 (2012).
- ⁵⁰Z. Y. Yang, Y. H. Chen, B. H. Liao, and K. P. Chen, “Room temperature fabrication of titanium nitride thin films as plasmonic materials by high-power impulse magnetron sputtering,” *Opt. Mater. Express* **6**(2), 540 (2016).
- ⁵¹J. Judek, P. Wróbel, P. P. Michałowski, M. Ożga, B. Witkowski, A. Seweryn *et al.*, “Titanium nitride as a plasmonic material from near-ultraviolet to very-long-wavelength infrared range,” *Materials* **14**(22), 7095 (2021).
- ⁵²P. R. West, S. Ishii, G. V. Naik, N. K. Emani, V. M. Shalae, and A. Boltasseva, “Searching for better plasmonic materials,” *Laser Photonics Rev.* **4**(6), 795–808 (2010).
- ⁵³E. Lewin, D. Loch, A. Montagne, A. P. Ehasarian, and J. Patscheider, “Comparison of Al–Si–N nanocomposite coatings deposited by HiPIMS and DC magnetron sputtering,” *Surf. Coat. Technol.* **232**, 680–689 (2013).
- ⁵⁴H. Larhlimi, M. Makha, and J. Alami, “Effect of pulse configuration on the reactive deposition of TiN coatings using HiPIMS,” *Surf. Coat. Technol.* **473**, 130024 (2023).

- ⁵⁵D. Horwat and A. Anders, "Compression and strong rarefaction in high power impulse magnetron sputtering discharges," *J. Appl. Phys.* **108**(12), 123306 (2010).
- ⁵⁶S. M. Rossmagel, "Magnetron plasma diagnostics and processing implications," *J. Vac. Sci. Technol. A* **6**(3), 1821–1826 (1988).
- ⁵⁷D. Gall, S. Kodambaka, M. A. Wall, I. Petrov, and J. E. Greene, "Pathways of atomistic processes on TiN(001) and (111) surfaces during film growth: An *ab initio* study," *J. Appl. Phys.* **93**(11), 9086–9094 (2003).
- ⁵⁸P. B. Barna, M. Adamik, G. Sáfrán, B. Pécz, A. Bergauer, and H. Bangert, "Peculiar lamellar structure in Al single crystals grown in oxygen-doped Al and Al–Sn thin films," *Phys. Status Solidi A* **146**(1), 317–324 (1994).
- ⁵⁹C. C. Chang, J. Nogan, Z. P. Yang, W. J. M. Kort-Kamp, W. Ross, T. S. Luk *et al.*, "Highly plasmonic titanium nitride by room-temperature sputtering," *Sci. Rep.* **9**(1), 15287 (2019).
- ⁶⁰G. V. Naik, B. Saha, J. Liu, S. M. Saber, E. A. Stach, J. M. K. Irudayaraj *et al.*, "Epitaxial superlattices with titanium nitride as a plasmonic component for optical hyperbolic metamaterials," *Proc. Natl. Acad. Sci. U. S. A.* **111**(21), 7546–7551 (2014).
- ⁶¹R. Bower, D. A. L. Loch, E. Ware, A. Berenov, B. Zou, P. Hovsepian *et al.*, "Complementary metal–oxide–semiconductor compatible deposition of nano-scale transition-metal nitride thin films for plasmonic applications," *ACS Appl. Mater. Interfaces* **12**(40), 45444–45452 (2020).
- ⁶²L. Mascaretti, T. Barman, B. R. Bricchi, F. Münz, A. Li Bassi, Š Kment *et al.*, "Controlling the plasmonic properties of titanium nitride thin films by radiofrequency substrate biasing in magnetron sputtering," *Appl. Surf. Sci.* **554**, 149543 (2021).
- ⁶³M. Nieborek, C. Jastrzębski, T. Płociński, P. Wróbel, A. Seweryn, and J. Judek, "Optimization of the plasmonic properties of titanium nitride films sputtered at room temperature through microstructure and thickness control," *Sci. Rep.* **14**(1), 5762 (2024).
- ⁶⁴H. Reddy, U. Guler, Z. Kudyshev, A. V. Kildishev, V. M. Shalaev, and A. Boltasseva, "Temperature-dependent optical properties of plasmonic titanium nitride thin films," *ACS Photonics* **4**(6), 1413–1420 (2017).